



High carrier mobility in graphene doped using a monolayer of tungsten oxyselenide

Min Sup Choi^{1,2,9}, Ankur Nipane^{3,9}, Brian S. Y. Kim^{1,9}, Mark E. Ziffer⁴, Ipshita Datta³, Abhinandan Borah³, Younghun Jung¹, Bumho Kim¹, Daniel Rhodes¹, Apoorv Jindal⁵, Zachary A. Lampert³, Myeongjin Lee², Amirali Zangiabadi⁶, Maya N. Nair⁷, Takashi Taniguchi⁸, Kenji Watanabe⁸, Ioannis Kymissis³, Abhay N. Pasupathy⁵, Michal Lipson³, Xiaoyang Zhu⁴, Won Jong Yoo², James Hone¹✉ and James T. Teherani³✉

Doped graphene could be of use in next-generation electronic and photonic devices. However, chemical doping cannot be precisely controlled in the material and leads to external disorder that diminishes carrier mobility and conductivity. Here we show that graphene can be efficiently doped using a monolayer of tungsten oxyselenide (TOS) that is created by oxidizing a monolayer of tungsten diselenide. When the TOS monolayer is in direct contact with graphene, a room-temperature mobility of 2,000 cm² V⁻¹ s⁻¹ at a hole density of 3 × 10¹³ cm⁻² is achieved. Hole density and mobility can also be controlled by inserting tungsten diselenide interlayers between TOS and graphene, where increasing the layers reduces the disorder. With four layers, a mobility value of around 24,000 cm² V⁻¹ s⁻¹ is observed, approaching the limit set by acoustic phonon scattering, resulting in a sheet resistance below 50 Ω sq⁻¹. To illustrate the potential of our approach, we show that TOS-doped graphene can be used as a transparent conductor in a near-infrared (1,550 nm) silicon nitride photonic waveguide and ring resonator.

Doping techniques that control the carrier density of a material over a wide range are crucial for fabricating advanced electronic and photonic devices^{1–3}. For graphene, doping is used to achieve high conductivity and tunable work functions, which are necessary for use in transparent electrodes and near-infrared (IR) and mid-IR photonics^{4,5}. However, conventional doping techniques, such as ion implantation, are ineffective for graphene and other two-dimensional (2D) materials⁶. Instead, surface charge transfer doping is typically used, and hole doping with nitrogen dioxide can, for example, achieve a hole density of 2×10^{12} cm⁻² and sheet resistance of around 300 Ω sq⁻¹ (ref. 7). Wet chemical doping using a variety of inorganic and organic dopants has also been explored, delivering carrier densities of >math>5 \times 10^{12}</math> cm⁻² and sheet resistances between 150 and 200 Ω sq⁻¹ (refs. 8–10). However, chemical doping can suffer from poor long-term stability and large device-to-device variability^{10,11}, and it introduces considerable charge disorder that limits the carrier mobility to below 1,000 cm² V⁻¹ s⁻¹. Solid-state dopants have the advantages of high repeatability, compatibility with complementary metal–oxide–semiconductor processes and long-term stability; non-stoichiometric insulators, such as SiN_x and AlO_x (refs. 12,13), have been used to optimize charge injection in 2D semiconductors. However, the doping approach has not been widely explored with graphene.

In this Article, we report low-disorder, tunable high-density doping of graphene using a monolayer of the solid-state oxide of tungsten oxyselenide (TOS), which is created via the room-temperature (RT), ultraviolet (UV)–ozone oxidation of tungsten diselenide

(WSe₂). The high-work-function TOS induces a mismatch-induced charge transfer with the nearby graphene layer. The oxidation process, which has been previously shown to be self-limiting¹⁴, allows layer-by-layer control and low disorder compared with other oxidation techniques; further, by starting from a crystalline layered source, charge disorder is reduced¹⁵. We show that the TOS layer induces a hole density of above 3 × 10¹³ cm⁻² in a neighbouring graphene layer, which has a high mobility of 2,000 cm² V⁻¹ s⁻¹ and sheet resistance of 118 Ω sq⁻¹. When the TOS is separated from graphene by WSe₂, the mobility rises further, similar to modulation doping in III–V semiconductor heterostructures, where the separation reduces impurity scattering¹⁶, showing phonon-limited mobility and a reduced sheet resistance of 48 Ω sq⁻¹. Doped graphene is also highly transparent in the IR, and we show that near-ideal transmittance (99.2%) and low insertion loss (0.012 dB μm⁻¹) at IR frequencies is possible using the TOS-doped graphene in a silicon nitride (SiN) photonic waveguide and ring resonator.

Electrical and Raman characterization of TOS-doped graphene

Figure 1a shows the process flow of fabricating TOS-doped monolayer graphene. The device is fabricated by first stacking monolayer WSe₂ (1L-WSe₂), graphene and bottom hexagonal boron nitride (hBN) using a polycaprolactone (PCL) polymer-based dry-transfer process¹⁷. The heterostructure is then etched into Hall bar structures for the accurate extraction of carrier densities and conductivities of graphene, with edge-contacted metal electrodes (Cr/Au)

¹Department of Mechanical Engineering, Columbia University, New York, NY, USA. ²SKKU Advanced Institute of Nano Technology, Sungkyunkwan University, Suwon, Korea. ³Department of Electrical Engineering, Columbia University, New York, NY, USA. ⁴Department of Chemistry, Columbia University, New York, NY, USA. ⁵Department of Physics, Columbia University, New York, NY, USA. ⁶Department of Applied Physics and Applied Mathematics, Columbia University, New York, NY, USA. ⁷Nanoscience Initiative, Advanced Science Research Center, CUNY, New York, NY, USA. ⁸National Institute for Materials Science, Tsukuba, Japan. ⁹These authors contributed equally: Min Sup Choi, Ankur Nipane, Brian S. Y. Kim. ✉e-mail: jh2228@columbia.edu; j.teherani@columbia.edu

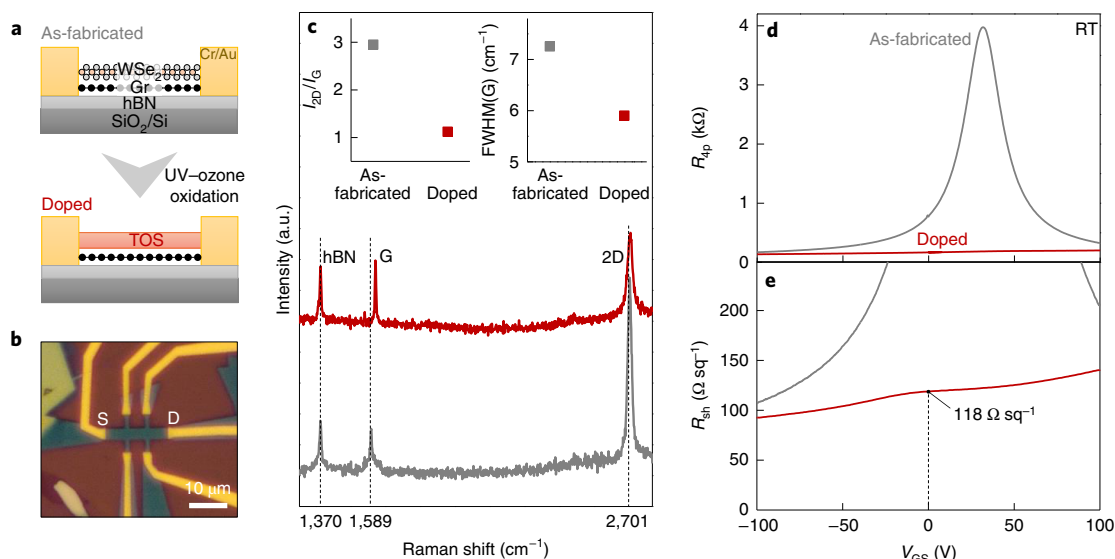


Fig. 1 | Electrical and Raman characterization of TOS-doped graphene. **a**, Device structure at different steps in the measurement process. UV-ozone oxidation only oxidizes the topmost monolayer WSe_2 into monolayer TOS, whereas the underlying graphene layer remains intact and gets heavily p-doped. **b**, Optical image of the TOS-doped graphene devices with Hall bar geometry. S and D represent the source and drain electrodes, respectively. **c**, Raman characterization of the graphene device showing blueshifts in the G and 2D peaks after oxidation, indicative of hole doping. Note that the hBN peak was used as a reference for calculating the peak shifts. The insets show a clear reduction in I_{2D}/I_G and FWHM of the G peak after oxidation. **d**, Four-point resistance R_{4p} as a function of V_{GS} for TOS-doped graphene before and after doping. Dirac peak shifts from V_{GS} of 30 V to beyond our measurement range after doping, indicative of the ultrahigh p-type doping of graphene. **e**, Sheet resistance R_{sh} of TOS-doped graphene showing $118 \Omega \text{sq}^{-1}$ at zero gate-bias voltage.

formed using standard lithography processes (Fig. 1b)¹⁸. Finally, the monolayer WSe_2 is oxidized into monolayer TOS at RT by exposing the sample to ozone under UV illumination for 30 min (Methods provides further device fabrication and UV-ozone oxidation details). In particular, the combination of UV and ozone is important as UV exposure creates local surface defects that facilitate the oxidation of the topmost WSe_2 layer on subsequent ozone exposure at RT. We note that this is in contrast to earlier studies utilizing only ozone without any UV exposure, which required an elevated temperature together with longer exposure time to completely oxidize the topmost WSe_2 layer¹⁹. We also note that another added benefit of our TOS-doping method is the self-cleaning nature of UV-ozone oxidation, resulting in the reduction in surface roughness and suppression of hysteresis arising from carrier (de-)trapping at the surface states formed by the polymer residue after oxidation (Supplementary Figs. 1–3)²⁰.

We first determine the type of carrier induced in our TOS-doped monolayer graphene using Raman spectroscopy, as shown in Fig. 1c. We find a clear blueshift in both G and 2D peaks (18.1 and 4.3cm^{-1} , respectively) to their original positions in pristine graphene²¹, which indicates that graphene becomes hole doped. This is corroborated by the I_{2D}/I_G ratio getting reduced by threefold and full-width at half-maximum (FWHM) of the G peak reduced from 7.3 to 5.9cm^{-1} after oxidation (Fig. 1c, inset). Four-probe resistance (R_{4p}) of graphene as a function of the back-gate bias (V_{GS}) at RT also shows a large shift in the Dirac peak from $V_{GS} = 30 \text{V}$ to beyond the measurement range after the formation of the TOS layer (Fig. 1d). This, together with R_{4p} decreasing with the negative bias voltage, clearly indicates that an ultrahigh density of holes is induced in graphene. As a result, the RT sheet resistance (R_{sh}) of our TOS-doped graphene shows a low value of $\sim 118 \Omega \text{sq}^{-1}$ at zero gate-bias voltage. Note that the weak secondary peak shown in R_{sh} can be attributed to small spatial inhomogeneity in the sample or formation of the moiré

potential from an unintentional atomic alignment of graphene with the bottom hBN (ref. 22). We further note that any contribution of the TOS layer to the measured conductivity can be ruled out by independent electrical measurements, which confirm that it is insulating (Supplementary Fig. 4).

Structural characterization of monolayer TOS

To gain further insight into the nature of the TOS layer, we investigate its structural properties using selected-area electron diffraction (SAED), as shown in Fig. 2. Figure 2b shows the SAED patterns of 1L- WSe_2 flake after oxidation, indicating the complete disappearance of hexagonal symmetry along the $[0001]$ zone axis. This suggests that the resultant TOS layer is amorphous. However, few-layer WSe_2 shows hexagonal single-crystal diffraction patterns even after oxidation, as shown in Fig. 2c,d, confirming that the UV-ozone oxidation process presented in our work is self-limiting in nature and thus the underlying WSe_2 layers remain in the pristine form (Supplementary Fig. 5 shows the transmission electron microscopy images of monolayer and few-layer WSe_2). The self-limited nature of our oxidation process is further corroborated by the energy-dispersive X-ray spectroscopy measurements of 1L- WSe_2 that show the presence of selenium atoms even after oxidation (Supplementary Table 1). We note that this self-limited nature allows for the repeated oxidation and etching of multilayer WSe_2 flake in a monolayer-by-monolayer fashion (Supplementary Fig. 1)¹⁴. On the atomistic level, this indicates that the TOS layer acts as a high diffusion barrier, preventing further penetration of ozone molecules into the underlying layers²³.

Figure 2e,f shows the X-ray photoelectron spectroscopy (XPS) spectra of the core levels of W 4f and Se 3d before and after the oxidation of chemical vapour deposition (CVD)-grown monolayer WSe_2 . We find a dominant formation of multivalent oxidation states of W (W^{5+} and W^{6+}) after oxidation, which verifies that 1L-TOS is

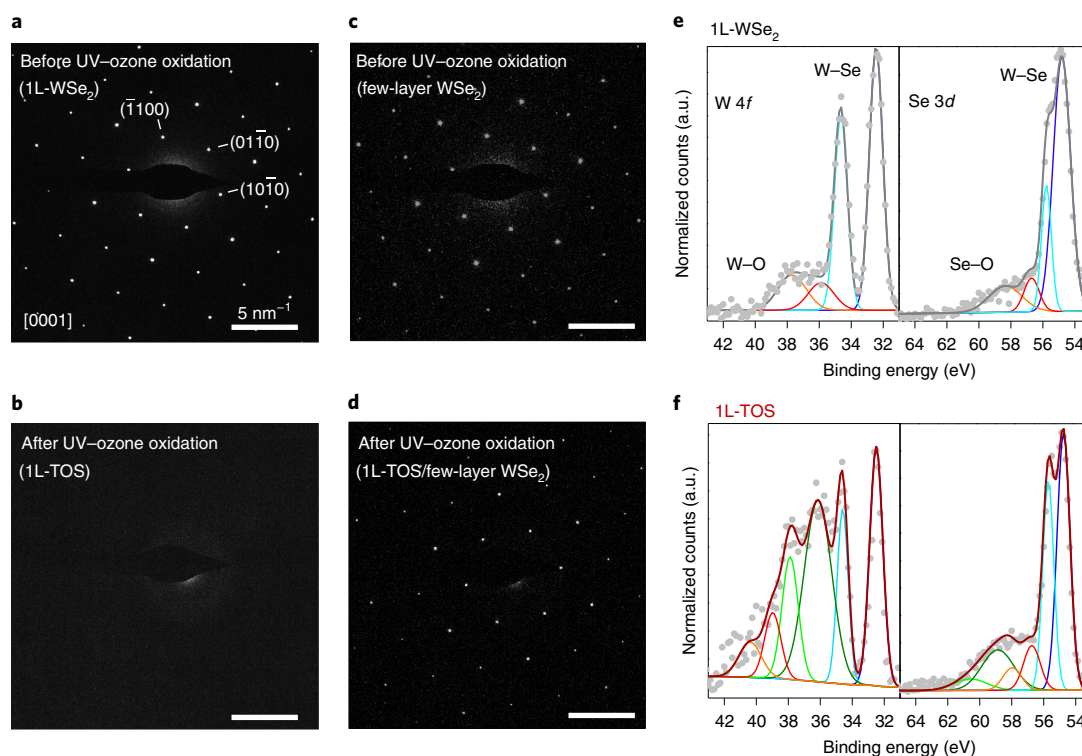


Fig. 2 | Structural characterization of monolayer TOS. **a, b**, SAED patterns of 1L-WSe₂ before (**a**) and after (**b**) the UV-ozone oxidation process. **c, d**, SAED patterns of few-layer WSe₂ before (**c**) and after (**d**) the UV-ozone oxidation process. Scale bars in **a–d**, 5 nm⁻¹. Single-crystal diffraction patterns with the [0001] zone axis are visible before UV-ozone oxidation and are completely removed after the UV-ozone oxidation process, indicating the amorphous nature of the TOS layer. In contrast, few-layer WSe₂ still shows crystalline patterns even after oxidation, indicating a self-limiting process. **e, f**, XPS characterization of 1L-WSe₂ (**e**) and 1L-TOS (**f**) indicating the W 4*f* and Se 3*d* peaks, respectively. A comparison of W 4*f* peaks shows the creation of multivalent oxidation states of W (W⁵⁺ and W⁶⁺) in the TOS layer, confirming the sub-stoichiometric nature of the TOS layer. The coloured lines show deconvoluted Gaussian peaks fit to the data. For W 4*f*, the doublet peak of W⁴⁺ is indicated by light blue (4*f*_{7/2}) and dark blue (4*f*_{5/2}). For Se 3*d*, the doublet peak of Se²⁻ is indicated by light blue (3*d*_{5/2}) and dark blue (3*d*_{3/2}). Multivalent oxidation states are shown in light/dark red and green lines.

sub-stoichiometric. Note that weak W–O and Se–O signals present before oxidation are presumably attributed to intrinsic defects present in the CVD-grown samples. We further note that defects in the amorphous nature of the TOS layer can cause surface adsorption of water and oxygen molecules, leading to time-dependent degradation²⁴. Supplementary Fig. 6 depicts the poly(methyl methacrylate) (PMMA) encapsulation layer as a potential solution to prevent this degradation. A slight initial decrease in the zero-gate bias hole density (p) of our TOS-doped graphene to $7 \times 10^{12} \text{ cm}^{-2}$ immediately after PMMA encapsulation can be attributed to the chemical reaction with a solvent at a high baking temperature of 180 °C. However, p remains nominally unchanged thereafter (~14% decrease in p over one month), showing the enhanced stability of our TOS-doping method.

Tunable carrier density and mobilities in TOS-doped graphene with WSe₂ interlayers

Figure 3a shows the measured p of TOS-doped graphene extracted from Hall effect measurements (Supplementary Fig. 7). We first focus on the case where the TOS is directly in contact with graphene. We find that the hole density is $3.2 \times 10^{13} \text{ cm}^{-2}$ at $V_{\text{GS}} = 0 \text{ V}$, consistent with the estimate from the Raman measurements. Applying V_{GS} can further tune p up to $3.7 \times 10^{13} \text{ cm}^{-2}$, demonstrating that the back-gate capacitance is electrostatically decoupled from the top TOS layer. This doping level is equivalent to ~1% of the graphene atomic density ($3.82 \times 10^{15} \text{ cm}^{-2}$), and it is similar to the maximum achievable value in silicon using substitutional doping²⁵. The doping level is also beyond what can be achieved by electrostatic gating

through solid dielectrics. For example, a graphite back-gated structure with an hBN dielectric can only achieve carrier densities of the order of $\sim 6 \times 10^{12} \text{ cm}^{-2}$ in graphene²⁶, and a perfect dielectric with a high electrical-breakdown dielectric strength of 1 V nm^{-1} can only accumulate $\sim 2 \times 10^{13} \text{ cm}^{-2}$.

The self-limiting nature of the oxidation process provides a straightforward method to tune the induced hole density. When multilayer WSe₂ is utilized, the top layer is converted to TOS and the remaining layers remain pristine, increasing the separation between the dopant layer and the channel. As we vary the interlayer WSe₂ thickness from one to four layers, the induced p decreases monotonically to $0.4 \times 10^{13} \text{ cm}^{-2}$ (Fig. 3a and Supplementary Fig. 8 (1.5 K)), and remains additionally tunable by the back gate. The corresponding Fermi energy (E_{F}) can be extracted using the relation

$$E_{\text{CNP}} - E_{\text{F}} = \hbar v_{\text{F}} \sqrt{\pi p}, \quad (1)$$

where E_{CNP} is the energy of the charge neutrality point (Dirac point), \hbar is the reduced Planck constant and v_{F} is the Fermi velocity in graphene (10^6 m s^{-1}). We find that E_{F} can be tuned from -0.1 to -0.7 eV , by simply changing the WSe₂ layer number together with the back gate (Fig. 3b).

We show the measured sheet resistance of graphene in Fig. 3c. At zero back-gate voltage, the TOS-graphene sample shows a R_{sh} of $118 \Omega \text{ sq}^{-1}$. For comparison, undoped graphene has R_{sh} of the order of a few $\text{k}\Omega \text{ sq}^{-1}$ and state-of-the-art chemically doped graphene has R_{sh} of $\sim 140 \Omega \text{ sq}^{-1}$ (ref. 4), illustrating the superiority of our doping method. Remarkably, for the three-interlayer and four-interlayer

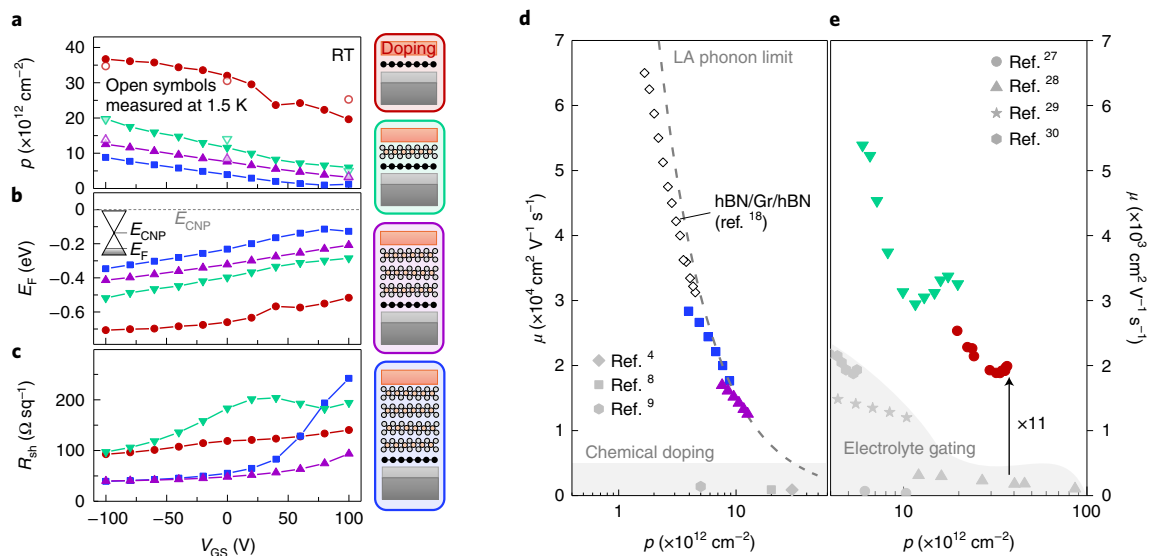


Fig. 3 | Tuning carrier density and mobilities in TOS-doped graphene with WSe₂ interlayers. **a–c**, Hole density (**a**), corresponding Fermi level of graphene with respect to E_{CNP} (**b**) and sheet resistance as a function of back-gate bias extracted from Hall effect measurements (**c**). Increasing the number of WSe₂ interlayers between TOS doping and graphene reduces the hole density in graphene as depicted in the right insets, which illustrate the device structures of corresponding coloured data points in **a–c**. High hole-doping densities push the Fermi level deep into the valence band, as shown in the inset of **b**. **d,e**, Hole mobility as a function of hole density for TOS-doped graphene with WSe₂ interlayers at RT compared with the mobilities with chemical doping (**d**) and electrolyte gating (**e**). TOS-doped graphene with 3L-WSe₂ and 4L-WSe₂ interlayers extend the LA phonon-limited hole mobility, previously achieved in hBN-encapsulated graphene (black points), to higher hole densities. These mobilities are substantially higher than other chemical doping techniques providing similar doping densities, highlighted in the bottom grey zone. At extremely high hole densities for TOS-doped graphene without and with 1L-WSe₂ interlayer, our work shows a notable (>10 times) mobility improvement compared with electrolyte gating.

samples, R_{sh} is even smaller, falling below $50 \Omega \text{sq}^{-1}$ (Supplementary Fig. 9). This indicates an increase in carrier mobility that more than offsets the reduced carrier density.

To explore the electrical performance of TOS-doped graphene in more detail, we plot the carrier mobility (at RT) derived from the measured sheet resistance and carrier density, as shown in Fig. 3d,e. With no interlayer WSe₂, the mobility is $\sim 2,000 \text{ cm}^2 \text{V}^{-1} \text{s}^{-1}$, more than an order of magnitude higher than that achieved in graphene with a similar high carrier density induced by either chemical doping^{4,8,9} or electrolyte gating^{27–30}. In spite of this dramatic improvement, the mobility still falls below the limit predicted from acoustic phonon scattering, indicating dominant scattering from charged impurities. The density of such impurities can be estimated from the measured low-temperature mobility $\mu \approx 20(e/hp_{\text{imp}})$, where p_{imp} is the impurity density, h is the Planck constant and e is the elementary charge (Supplementary Fig. 8b,c)³¹. From this relation, we estimate $p_{\text{imp}} \approx 4.6 \times 10^{11} \text{ cm}^{-2}$, well below that of electrolyte-gated graphene (ranging from 6×10^{12} to $1 \times 10^{13} \text{ cm}^{-2}$) (ref. ³²). This indicates that charge disorder in the TOS layer is much lower than other dopants.

With the insertion of interlayer WSe₂, the mobility improves dramatically, reaching values of $\sim 17,000 \text{ cm}^2 \text{V}^{-1} \text{s}^{-1}$ for the three-interlayer sample and $\sim 24,000 \text{ cm}^2 \text{V}^{-1} \text{s}^{-1}$ for the four-interlayer sample at zero gate-bias voltage. Remarkably, these values are at the limit set by longitudinal acoustic (LA) phonon scattering¹⁸. This indicates that three layers of WSe₂ ($\sim 2 \text{ nm}$) can screen the charged impurities in the TOS layer such that impurity scattering is reduced by more than an order of magnitude. This is consistent with previous studies showing that the charged-impurity scattering rate rapidly decreases as a function of the distance between the impurities and graphene layer³³. Mobility improvement achieved in this way is analogous to the modulation-doping technique in conventional semiconductor heterostructures, where the physical separation of dopant from the active channel drastically increases carrier mobility by minimizing impurity scattering by dopant atoms¹⁶.

To understand the origin of charge transfer between TOS and graphene, we focus on two important electrostatic boundary conditions imposed in our devices in equilibrium: the constant Fermi level E_{F} across the entire system and the continuous vacuum level without any discontinuities. We first note that the charge neutrality point of graphene lies deep in the bandgap of WSe₂; therefore, WSe₂ can be effectively treated as a dielectric³⁴. Therefore, the resultant electrostatic boundary condition in our TOS-doped graphene with interlayer WSe₂ can be expressed in terms of the work function Φ of the individual layers as

$$\Phi_{\text{TOS}} = \Phi_{\text{Gr}} + pt/\epsilon, \quad (2)$$

where Φ_{TOS} (Φ_{Gr}) is the work function of TOS (graphene) with respect to the vacuum level, t is the distance between graphene and TOS and ϵ is the dielectric constant of WSe₂. Here we use $\epsilon = 3.8$ (ref. ³⁵). The final term in equation (2) is the potential drop developed across TOS and graphene as a result of charge transfer, which can be determined from Poisson's equation³⁶. From equation (2), we find that our model effectively fits our data for p in TOS-doped graphene as a function of t (Fig. 4a), indicating that charge transfer is dictated by work-function mismatch between the two layers. Note that the extracted Φ_{TOS} ($\sim 5.6 \text{ eV}$) is in good agreement with previous studies on non-stoichiometric tungsten oxides³⁷.

To validate our model of work-function-mediated charge transfer, we study the TOS-doped graphene devices with different stacking orders of graphene (Gr) and TOS layer (Gr/TOS and TOS/Gr) as well as with different insulating interlayers (TOS/2L-hBN/Gr; Supplementary Fig. 10). The Raman spectra clearly show the hole doping of graphene irrespective of the stacking order or type of insulating interlayer (Fig. 4b)³⁸. This not only verifies the work-function-mediated charge transfer but also rules out the possibility of doping due to fixed dipoles, as seen for self-assembled monolayers and ferroelectric insulators^{39,40}. The densities extracted

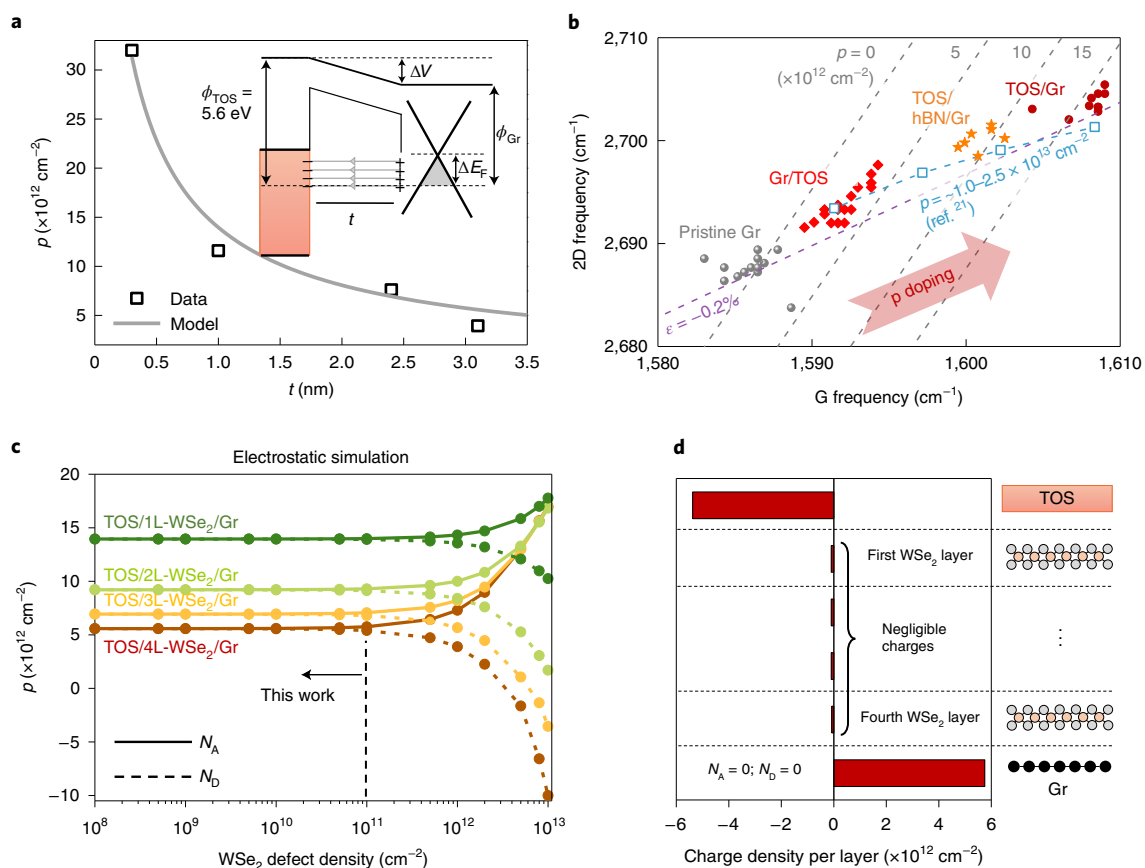


Fig. 4 | Work-function-mediated charge transfer in TOS-doped graphene. **a**, Graphene hole density p as a function of distance t between the TOS layer and graphene. Our model based on work-function-mediated charge transfer provides excellent fits to the experimental data. **b**, Raman map of 2D versus G-peak frequencies for pristine graphene (grey), graphene on 1L-TOS (red), 1L-TOS on graphene with 2L-hBN spacer (orange) and 1L-TOS on graphene (dark red). The grey and purple dotted lines indicate shift in the G and 2D peaks for different carrier density and strain values, respectively³⁸. A clear blueshift obtained from the G and 2D peaks in graphene along the $\epsilon = -0.2\%$ line can be seen after TOS doping, irrespective of the TOS location. The shifts are in good agreement with a previous work on p-type carrier modulation in graphene devices (shown in sky blue)²¹. **c**, Self-consistent electrostatic simulation of induced hole density in TOS-doped graphene as a function of defect density for different thicknesses of WSe₂ interlayer. **d**, The same simulation for 4L-WSe₂ interlayer device shows negligible charges in the WSe₂ interlayers compared with the bottom graphene.

from the Raman shifts, namely, $>2.5 \times 10^{13} \text{ cm}^{-2}$ for the TOS/graphene sample, $\sim 1 \times 10^{13} \text{ cm}^{-2}$ for the graphene/TOS sample and $\sim 2 \times 10^{13} \text{ cm}^{-2}$ for the TOS/2L-hBN/graphene sample, are in good agreement with our Hall effect measurements²¹. A slight decrease in doping density of the graphene/TOS sample (compared with TOS/graphene) can be attributed to the stacking and cleaning processes at elevated temperatures.

The proposed doping mechanism indicates that TOS can be an effective hole dopant for many other materials with suitable work-function mismatch. We test this by interfacing TOS with semiconductors spanning various dimensions—one-dimensional semiconductor (single-walled carbon nanotube (SWCNT)), 2D semiconductor (4L-WSe₂) and three-dimensional organic semiconductor (dinaphtho[2,3-b:2',3'-f]thieno[3,2-b]thiophene (DNTT)) (fabrication details are provided in Methods). Supplementary Figs. 11–13 clearly show that hole densities increase in these systems after the placement of TOS on their surface, indicating that high-work-function TOS can universally p-dope a wide range of materials.

We next perform self-consistent electrostatic simulations using the extracted Φ_{TOS} value of $\sim 5.6 \text{ eV}$ to gain a further insight into the role of the WSe₂ interlayer in the charge transfer process (simulation details can be found in our previous work⁴¹). The additional material parameters are provided in Supplementary Table 2. Specifically,

we study the effect of defects in WSe₂ on the resultant p in graphene at RT, as shown in Fig. 4c. Here we assume that the defects are either acceptors (with density N_A , solid line) or donors (with density N_D , dashed line). For defect densities lower than $5 \times 10^{11} \text{ cm}^{-2}$, our simulations show that p can be well understood in terms of equation (2) for any number of WSe₂ interlayers. However, p departs from equation (2) at higher defect densities due to additional charge transfer from acceptors (donors) in WSe₂ to graphene, which further decreases (increases) the resultant hole density in graphene. In our studies, we use high-purity flux-grown WSe₂ with low defect densities ($<10^{11} \text{ cm}^{-2}$) (ref. 42). Therefore, the simulations support the model of charge transfer dictated by work-function mismatch and validate the assumption of treating interlayer WSe₂ as a simple dielectric. In this low-defect-density limit, our simulations further show that the induced charge densities in the WSe₂ interlayer are orders of magnitude lower than those in graphene (Fig. 4d and Supplementary Fig. 14). This indicates that the electrical characteristics of our devices are dominated by the bottom graphene layer with negligible WSe₂ contribution.

Optical characterization of TOS-doped graphene

We next illustrate the potential of TOS-doped graphene in optoelectronic applications. One immediate advantage of our technique is the ability to strongly suppress interband absorption for

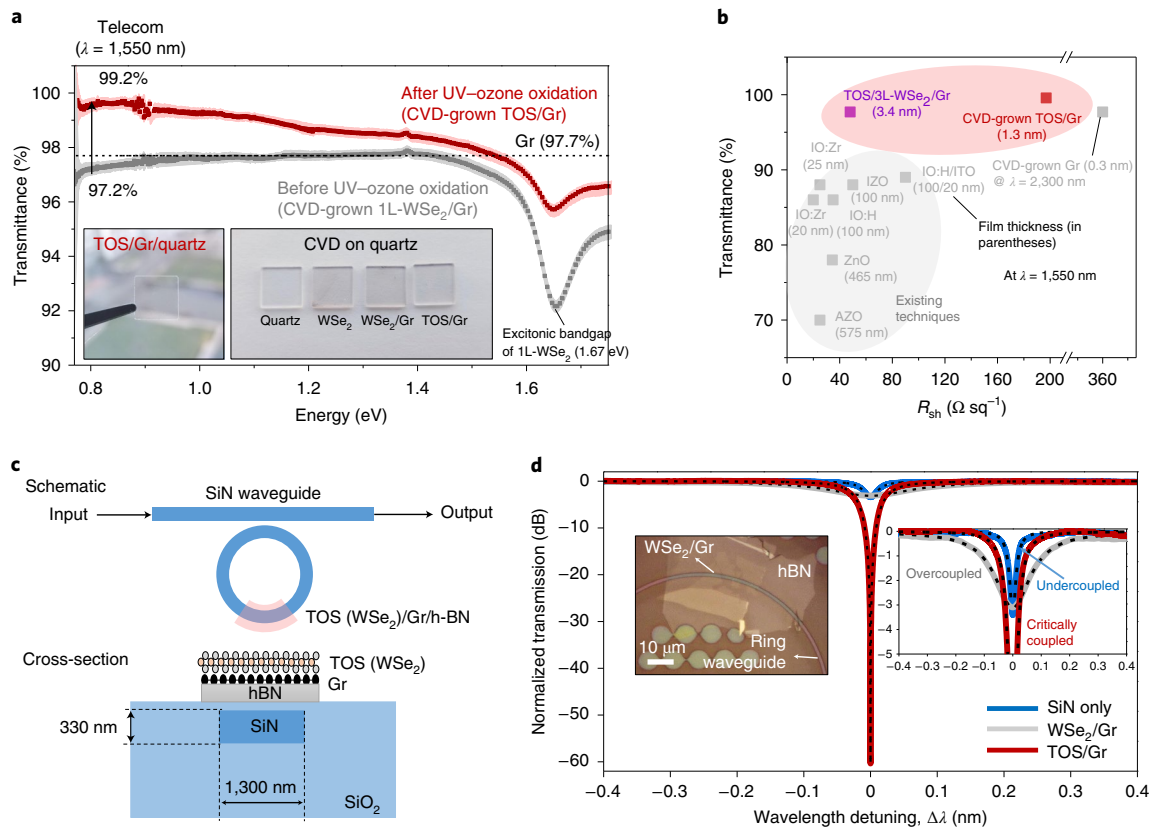


Fig. 5 | Optical properties of TOS-doped graphene. **a**, Transmittance of CVD-grown 1L-WSe₂ on graphene before and after UV-ozone oxidation. The shaded area indicates the standard deviation. The dashed line indicates the transmittance of intrinsic graphene (97.7%). Before UV-ozone oxidation, the transmittance for photon energies less than 1.4 eV remains around graphene's intrinsic absorption. An excitonic bandgap peak of WSe₂ is also seen at 1.67 eV. After UV-ozone oxidation, the peak is reduced along with an increment in the transmittance from 97.2% to 99.2% at telecommunication wavelength (1,550 nm). The insets show different CVD stacks on a quartz substrate to compare the transparency in the visible regime. **b**, Comparison of optical transmission at 1,550 nm for TOS-doped Gr with widely used transparent conducting films as a function of sheet resistance. Thickness of the films is indicated in the parentheses. **c**, Top view and cross-sectional schematic of a microring resonator with TOS(WSe₂)/Gr/hBN composite stack on planarized SiN waveguide. **d**, Normalized resonator transmission spectra of the planarized SiN ring configuration before transfer (blue), after transfer (grey) and after UV-ozone oxidation (red) of the stack. The black dashed lines indicate the numerical fit of the ring-resonator equation with the measured transmission response of the ring resonator. Before transfer (blue), the ring resonator is in the undercoupled regime, where the ring resonator and bus waveguide exhibit weak coupling due to the ultralow-loss waveguides (2.326 dB cm⁻¹). After transfer (grey), the insertion loss in the composite SiN waveguides increases to 0.077 ± 0.014 dB μm^{-1} , which overcouples the ring resonator to the waveguide, causing considerable broadening of the resonator linewidth. The high loss in the ring can be attributed to undoped graphene. After UV-ozone oxidation, the transmission spectra exhibit a critical coupling condition, where insertion loss due to the stack is reduced by 85% to 0.012 ± 0.0022 dB μm^{-1} . The error range in the insertion loss measurement before and after oxidation arises due to uncertainty in the length of the stack transferred on the ring resonator (as shown in the inset).

photon energies up to $2E_F$ due to Pauli blocking⁵. Figure 5a shows the measured transmittance spectra of CVD-grown 1L-WSe₂/graphene films on quartz before and after UV-ozone oxidation (see Supplementary Fig. 15 and Methods for the detailed measurement setup). Before oxidation, the transmittance is near graphene's intrinsic value (97.7%) for photon energies less than 1.4 eV since the top WSe₂ is transparent in the near-IR region, and shows a dip at 1.67 eV that corresponds to the excitonic bandgap of WSe₂. In contrast, the near-IR transmittance notably improves after oxidation, increasing to 99.2% at telecommunication wavelengths ($\lambda \approx 1,550$ nm). From the transmittance data, we can infer that $E_F \approx 0.6$ eV for our TOS-doped graphene, in reasonable agreement with that from electrically measurements for the exfoliated sample discussed above (0.65 eV). Furthermore, the TOS-doped graphene is highly transparent even in the visible regime (Fig. 5a, insets) indicated by the reduction in the WSe₂ absorption peak. The weak presence of the excitonic peak is due to thickness inhomogeneity

in the top CVD-grown WSe₂ layer within the area of illumination (~6% of the area is covered by 2L-WSe₂, as shown in Supplementary Fig. 15c). Figure 5b shows that our TOS-doped graphene displays superior performance at telecommunication wavelength (1,550 nm) compared with other conventional transparent conducting films, including indium tin oxide (ITO), zinc-doped indium oxide (IZO), zirconium-doped indium oxide (IO:Zr), hydrogen-doped indium oxide (IO:H), zinc oxide (ZnO) and aluminium-doped zinc oxide (AZO)^{43–47}. In general, traditional transparent conductors suffer from a trade-off between transmittance and sheet resistance. In contrast, our CVD-grown TOS/Gr and exfoliated TOS/3L-WSe₂/Gr samples provide exceptionally high transmittance while maintaining a remarkably low sheet resistance, namely, >99% transmittance at $197 \Omega \text{sq}^{-1}$ and 97.7% at $48 \Omega \text{sq}^{-1}$, respectively. This highlights both intrinsic suppression of interband transitions in highly doped graphene and the ability of the TOS-doping technique to achieve high carrier density while maintaining high mobility.

Finally, we demonstrate the ability to utilize TOS-doped graphene as a transparent gate electrode and high-speed phase modulator in near-IR photonic circuits⁴⁸. We probe the optical response of TOS-doped graphene embedded on planarized low-loss SiN waveguides, in a microring resonator cavity (Fig. 5c; Methods provides the detailed fabrication processes). Notably, our planar photonic structure comprises a TOS/Gr/hBN/SiN composite waveguide with a strong optical-mode overlap compared with out-of-plane measurements. The normalized ring transmission spectra show that the bare low-loss cavity is weakly coupled to the straight waveguide (undercoupled regime), thereby yielding a low extinction of ~3 dB on resonance, with a narrow linewidth (Fig. 5d). After the transfer of WSe₂/Gr/hBN on the planarized SiN substrate, we extract an insertion loss of $0.077 \pm 0.014 \text{ dB } \mu\text{m}^{-1}$ in our composite waveguide from the optical response, as shown by the grey colour in Fig. 5d (Methods and Supporting Information provide the insertion loss extraction)⁴⁹. We attribute the high insertion loss to undoped graphene in the WSe₂/Gr/hBN stack, which causes the resonator linewidth to broaden considerably, increasing the cavity loss and overcoupling the waveguide to the cavity. The insertion loss is lowered by about 85% to $0.012 \pm 0.0022 \text{ dB } \mu\text{m}^{-1}$ after UV–ozone oxidation. The lowering of the insertion loss leads to the condition in which the coupling rate between the waveguide and ring resonator equals the optical decay rate in the cavity, thereby exhibiting a critically coupled resonance transmission response (Fig. 5d, red), where the extinction is ~60 dB with the spectral sharpening of the resonance. The magnified change in the in-plane transmission compared with the out-of-plane transmission (Fig. 5a) is attributed to the enhanced optical-mode overlap in the integrated photonic circuits. This low insertion loss of $0.012 \text{ dB } \mu\text{m}^{-1}$ uniquely places TOS-doped graphene as an ideal alternative to traditional transparent conducting materials such as ITO that has at least two orders of magnitude higher insertion loss ($1.6 \text{ dB } \mu\text{m}^{-1}$) with similar device geometries⁵⁰.

Conclusions

We have reported high-density p-type doping of graphene using work-function-mediated charge transfer from monolayer TOS, prepared by RT UV–ozone oxidation of monolayer WSe₂. TOS-doped graphene without any WSe₂ interlayers exhibits hole mobilities of $2,000 \text{ cm}^2 \text{ V}^{-1} \text{ s}^{-1}$, even at a hole density above $3 \times 10^{13} \text{ cm}^{-2}$, which resulted in an RT sheet resistance of $118 \Omega \text{ sq}^{-1}$. The carrier density can also be tuned and the mobility can be increased—up to the phonon-limited scattering rate—by inserting WSe₂ interlayers, with a minimum sheet resistance below $50 \Omega \text{ sq}^{-1}$. A self-consistent electrostatic model based on work-function mismatch can be used to describe the charge transfer mechanism, as well as the carrier density dependence on WSe₂ interlayer number. Our TOS-doped graphene also exhibits high optical transmittance (>99%) and low insertion loss ($0.012 \text{ dB } \mu\text{m}^{-1}$) at telecommunication wavelength. Our approach offers a promising doping method that could be used to incorporate van der Waals heterostructures into photonic circuits as a transparent gate electrode and a high-speed phase modulator for near-IR applications.

Methods

Fabrication and characterization of graphene device. WSe₂, graphene and hBN flakes were prepared on an SiO₂/Si substrate by mechanical exfoliation. The thickness of each flake was determined by the contrast difference in the optical microscopic images and Raman spectra. Only monolayer graphene was used, whereas the WSe₂ thickness varied from one layer (1L) to five layers (5L) to verify the layer dependence. The stacking of flakes was conducted by the dry-transfer method using PCL polymer at 50–58 °C to pick up flakes that are then transferred onto 285 nm SiO₂/Si at 80 °C to melt the polymer. To remove the polymer, the sample was annealed at 340 °C under a vacuum condition. Edge contacts were formed to the graphene layer by etching through the layers and subsequently depositing electron-beam (e-beam)-evaporated metal. Cr/Au (2/80 nm) contacts were deposited by e-beam evaporation after reactive-ion etching (RIE) of the

WSe₂, graphene and hBN layers with CHF₃ to form the edge contact. UV–ozone oxidation (Samco UV-2 system located in a class 100 cleanroom controlling humidity at <40% and temperature at <20 °C) was conducted at RT for 30 min at an oxygen flow rate of 3 l min^{-1} . The system has a separate discharge-type ozone generator and the generated ozone flows into the sample chamber underneath the UV-light source. The UV lamp is a mercury grid lamp with primary wavelengths of 254 and 185 nm and output power of $\sim 10 \text{ mW cm}^{-2}$. The chuck temperature was maintained at <50 °C during the oxidation process. Etching to remove the TOS was conducted using 1 M KOH diluted in deionized water followed by rinsing with deionized water and annealing in a vacuum at 300 °C. Electrical measurements were performed with both semiconductor parameter analyser (Keysight B1500A) and lock-in amplifiers (Stanford Research Systems SR830) connected to a cryostat containing a tunable perpendicular magnetic field under vacuum conditions.

Fabrication of SWCNT, WSe₂ and DNTT devices. *SWCNT device.* CNTs were grown on an SiO₂/Si substrate at 890 °C. The locations of SWCNTs were identified using scanning electron microscopy and atomic force microscopy scans. Cr/Pd (2/20 nm) contacts were then fabricated on select SWCNTs using the lift-off method. Here 1L-WSe₂ was transferred and subsequently oxidized after the initial electrical measurements of the SWCNT (without TOS) were completed.

WSe₂ device. In this case, 4L-WSe₂ was stacked on hBN using the same dry-transfer process used with graphene. E-beam evaporation and lift-off method were used to create the top surface contacts of Pd/Au (20/50 nm) to WSe₂. Electrical measurements of the same device before and after UV–ozone oxidation are presented in the manuscript.

DNTT device. Two devices were made on the same chip, one with TOS and one without TOS. To create the device with TOS, we first exfoliated 1L-WSe₂ on an SiO₂/Si substrate followed by lift-off metallization with Ti/Pd/Au (2/20/20 nm). Further, 1L-WSe₂ was converted into monolayer TOS through UV–ozone oxidation. Contacts were also concurrently patterned in areas without TOS to form the second device. Then, 40 nm DNTT was deposited via sublimation. The channel areas were defined by coating the sample with PMMA, patterning with e-beam lithography and etching away the semiconductor with SF₆ plasma, leaving the active channel area (Supplementary Fig. 13).

Transmittance measurements. The transmittance of 1L-WSe₂/Gr that was directly grown on a quartz substrate (purchased from 2D semiconductors) via CVD was measured under the ambient condition using a custom setup built around a Nikon TE-300 inverted microscope, as shown in Supplementary Fig. 15. The output of a tungsten halogen lamp was focused onto a 50 μm pinhole and an aspheric condenser lens to obtain collimated white light, which was focused at the sample plane through the quartz substrate using a long-working-distance ×50 objective (numerical aperture, 0.55). The transmitted light was collected with ×40 (numerical aperture, 0.60) objective focused at the sample plane from below and was sent to an *f*/4 (where *f* is the focal length) spectrograph (Princeton Instruments SpectraPro HRS-300) equipped with a cooled InGaAs array detector (Princeton Instruments PyLoN IR). Order-sorting filters were used to avoid higher-order diffraction signals. Transmittance was calculated by dividing the transmitted intensity measured on the sample by the transmitted intensity through a nearby blank area of quartz, with dark counts subtracted from both measurements. The system was optimized to ensure that the instrument error was <0.5% over the whole spectral range for each measurement, as indicated by the shaded area of the spectrum.

Fabrication of SiN photonic platform with TOS-doped graphene. To fabricate low-loss SiN waveguides, we use e-beam lithography to define 1,300-nm-wide waveguides on a stack of 360 nm plasma-enhanced-CVD-grown SiO₂ hard mask and 330-nm-high SiN, deposited using low-pressure CVD at 800 °C and annealed at 1,200 °C for 3 h on 4,170 nm thermally oxidized SiO₂. We use CHF₃/O₂ (52/2 s.c.c.m.) chemistry in an Oxford Plasmalab 100 ICP RIE system to etch the hard mask of 360 nm SiO₂ and subsequently use an optimized etch recipe of CHF₃/O₂/N₂ (47/23/7 s.c.c.m.) that uses a higher oxygen content reducing both polymerization and side-wall roughness. We use 360 nm SiO₂ as a sacrificial hard mask for etching SiN, since increasing the O₂ flow lowers the selectivity of etching. Following the etch, we deposit about 600 nm plasma-enhanced-CVD-grown SiO₂ on the waveguides. We planarize the SiO₂ to about 70–100 nm above the SiN waveguides using standard chemical planarization techniques to create a uniform surface for the transfer of the WSe₂/Gr/hBN stack on the ring resonator. Subsequently, a stack of 1L-WSe₂/1L-Gr/~20–25 nm hBN was transferred onto the planarized SiN waveguides using a PCL dry-transfer method. To remove the polymer, the sample was annealed at 340 °C under vacuum conditions. Finally, UV–ozone oxidation is performed to oxidize WSe₂ into TOS and to dope graphene. Notably, microring resonators allow the high-fidelity measurement of the optical propagation loss induced by TOS-doped graphene due to the enhanced sensitivity of a high-quality-factor (Q) cavity (~300,000 in our case) to small changes in phase and absorption.

Optical loss measurement and insertion loss estimation. We couple transverse-electric-polarized light from a tunable near-IR laser (~1,550–1,650 nm)

to the input of the SiN microring resonator (schematic shown in Fig. 5c) using a tapered single-mode fibre, which is then collected from the SiN ring output, using a similar tapered fibre. Transmission measurements were taken from the same device (1) before transfer to account for the insertion loss of planarized SiN substrates, (2) once after transfer to account for the insertion loss due to undoped graphene and (3) finally after UV–ozone oxidation to measure the propagation loss due to the composite waveguide with doped graphene. The original normalized transmission responses are shown in Supplementary Fig. 16. We normalize each ring transmission spectrum by the maximum transmission power at the output at wavelength detuning $\Delta\lambda$, where the cavity does not interact with the incoming light. We estimate the insertion loss by fitting the experimental normalized ring transmission to the theoretical ring transmission (T) obtained from the following resonator equation:

$$T = \left| 1 - \frac{\frac{2}{\tau_e}}{j(\omega - \omega_0) + \frac{1}{\tau_0} + \frac{1}{\tau_e}} \right|^2, \quad (3)$$

where $\frac{1}{\tau_e}$ is the decay rate (coupling rate) from the waveguide (bus) to the ring resonator, $\frac{1}{\tau_0}$ is the decay rate due to loss in the ring, and $\omega - \omega_0$ is the frequency detuning (ω_0 , the resonant frequency). The Q value of the ring resonator is related to τ_0 and α (insertion loss in the linear scale) through the equation $Q = \omega_0 \tau_0 \approx \frac{2\pi n_g}{\alpha \lambda_0}$, where n_g is the group index, $\omega_0 = \frac{2\pi c}{\lambda_0}$, c is the speed of light in vacuum and λ_0 is the resonant wavelength.

Data availability

The data that support the findings within this paper are available from the corresponding authors upon reasonable request.

Received: 14 December 2020; Accepted: 15 September 2021;
Published online: 22 October 2021

References

- Pierret, R. F. *Semiconductor Device Fundamentals* (Addison-Wesley, 1996).
- Seabaugh, A. C. & Zhang, Q. Low-voltage tunnel transistors for beyond CMOS logic. *Proc. IEEE* **98**, 2095–2110 (2010).
- Shen, L. et al. Ohmic contacts with ultra-low optical loss on heavily doped n-type InGaAs and InGaAsP for InP-based photonic membranes. *IEEE Photon. J.* **8**, 4500210 (2016).
- Ma, L.-P. et al. Pushing the conductance and transparency limit of monolayer graphene electrodes for flexible organic light-emitting diodes. *Proc. Natl Acad. Sci. USA* **117**, 25991–25998 (2020).
- Low, T. & Avouris, P. Graphene plasmonics for terahertz to mid-infrared applications. *ACS Nano* **8**, 1086–1101 (2014).
- Jena, D. & Konar, A. Enhancement of carrier mobility in semiconductor nanostructures by dielectric engineering. *Phys. Rev. Lett.* **98**, 136805 (2007).
- Schedin, F. et al. Detection of individual gas molecules adsorbed on graphene. *Nat. Mater.* **6**, 652–655 (2007).
- D'Arsi , L. et al. Stable, efficient p-type doping of graphene by nitric acid. *RSC Adv.* **6**, 113185–113192 (2016).
- Yager, T. et al. High mobility epitaxial graphene devices via aqueous-ozone processing. *Appl. Phys. Lett.* **106**, 063503 (2015).
- Mehta, A. N. et al. Understanding noninvasive charge transfer doping of graphene: a comparative study. *J. Mater. Sci.: Mater. Electron.* **29**, 5239–5252 (2018).
- Lee, H., Paeng, K. & Kim, I. S. A review of doping modulation in graphene. *Synthetic Met.* **244**, 36–47 (2018).
- Chen, K. et al. Air stable n-doping of WSe₂ by silicon nitride thin films with tunable fixed charge density. *APL Mater.* **2**, 092504 (2014).
- McClellan, C. J., Yalon, E., Smithe, K. K. H., Suryavanshi, S. V. & Pop, E. High current density in monolayer MoS₂ doped by AlO_x. *ACS Nano* **15**, 1587–1596 (2021).
- Nipane, A. et al. Damage-free atomic layer etch of WSe₂: a platform for fabricating clean two-dimensional devices. *ACS Appl. Mater. Interfaces* **13**, 1930–1942 (2021).
- Pang, C.-S. et al. Atomically controlled tunable doping in high-performance WSe₂ devices. *Adv. Electron. Mater.* **6**, 1901304 (2020).
- Dingle, R., St rmer, H. L., Gossard, A. C. & Wiegmann, W. Electron mobilities in modulation-doped semiconductor heterojunction superlattices. *Appl. Phys. Lett.* **33**, 665–667 (1978).
- Son, S. et al. Strongly adhesive dry transfer technique for van der Waals heterostructure. *2D Mater.* **7**, 041005 (2020).
- Wang, L. et al. One-dimensional electrical contact to a two-dimensional material. *Science* **342**, 614–617 (2013).
- Yamamoto, M. et al. Self-limiting layer-by-layer oxidation of atomically thin WSe₂. *Nano Lett.* **15**, 2067–2073 (2015).
- Wang, H., Wu, Y., Cong, C., Shang, J. & Yu, T. Hysteresis of electronic transport in graphene transistors. *ACS Nano* **4**, 7221–7228 (2010).
- Das, A. et al. Monitoring dopants by Raman scattering in an electrochemically top-gated graphene transistor. *Nat. Nanotechnol.* **3**, 210–215 (2008).
- Finney, N. R. et al. Tunable crystal symmetry in graphene–boron nitride heterostructures with coexisting moir  superlattices. *Nat. Nanotechnol.* **14**, 1029–1034 (2019).
- Sen, H. S., Sahin, H., Peeters, F. M. & Durgun, E. Monolayers of MoS₂ as an oxidation protective nanocoating material. *J. Appl. Phys.* **116**, 083508 (2014).
- Yamamoto, M., Nakaharai, S., Ueno, K. & Tsukagoshi, K. Self-limiting oxides on WSe₂ as controlled surface acceptors and low-resistance hole contacts. *Nano Lett.* **16**, 2720–2727 (2016).
- Wang, M. et al. Breaking the doping limit in silicon by deep impurities. *Phys. Rev. Appl.* **11**, 054039 (2019).
- Amet, F. et al. Composite fermions and broken symmetries in graphene. *Nat. Commun.* **6**, 5838 (2015).
- Dankler, M. et al. Graphene solution-gated field-effect transistor array for sensing applications. *Adv. Funct. Mater.* **20**, 3117–3124 (2010).
- Zhao, J. et al. Application of sodium-ion-based solid electrolyte in electrostatic tuning of carrier density in graphene. *Sci. Rep.* **7**, 3168 (2017).
- Hess, L. H. et al. High-transconductance graphene solution-gated field effect transistors. *Appl. Phys. Lett.* **99**, 033503 (2011).
- Brown, M. A., Crosser, M. S., Leyden, M. R., Qi, Y. & Minot, E. D. Measurement of high carrier mobility in graphene in an aqueous electrolyte environment. *Appl. Phys. Lett.* **109**, 093104 (2016).
- Adam, S., Hwang, E. H., Galitski, V. M. & Sarma, S. D. A self-consistent theory for graphene transport. *Proc. Natl Acad. Sci. USA* **104**, 18392–18397 (2007).
- Browning, A. et al. Evaluation of disorder introduced by electrolyte gating through transport measurements in graphene. *Appl. Phys. Express* **9**, 065102 (2016).
- Hwang, E. H., Adam, S. & Sarma, S. D. Carrier transport in two-dimensional graphene layers. *Phys. Rev. Lett.* **98**, 186806 (2007).
- Xu, Y. et al. Creation of moir  bands in a monolayer semiconductor by spatially periodic dielectric screening. *Nat. Mater.* **20**, 645–649 (2021).
- Ruta, F. L., Sternbach, A. J., Dieng, A. B., McLeod, A. S. & Basov, D. N. Quantitative nanoinfrared spectroscopy of anisotropic van der Waals materials. *Nano Lett.* **20**, 7933–7940 (2020).
- Sze, S. M. & Ng, K. K. *Physics of Semiconductor Devices* (John Wiley & Sons, 2006).
- Mews, M., Korte, L. & Rech, B. Oxygen vacancies in tungsten oxide and their influence on tungsten oxide/silicon heterojunction solar cells. *Sol. Energy Mater. Sol. Cells* **158**, 77–83 (2016).
- Lee, J. E., Ahn, G., Shim, J., Lee, Y. S. & Ryu, S. Optical separation of mechanical strain from charge doping in graphene. *Nat. Commun.* **3**, 1024 (2012).
- Nouchi, R. & Ikeda, K. I. Adsorbates as a charge-carrier reservoir for electrostatic carrier doping to graphene. *Appl. Phys. Express* **13**, 015005 (2020).
- Wu, G. et al. Programmable transition metal dichalcogenide homojunctions controlled by nonvolatile ferroelectric domains. *Nat. Electron.* **3**, 43–50 (2020).
- Borah, A., Sebastian, P. J., Nipane, A. & Teherani, J. T. An intuitive equivalent circuit model for multilayer van der Waals heterostructures. *IEEE Tran. Electron Devices* **65**, 4209–4215 (2018).
- Edelberg, D. et al. Approaching the intrinsic limit in transition metal diselenides via point defect control. *Nano Lett.* **19**, 4371–4379 (2019).
- Micallef, F. G. et al. Transparent conductors for mid-infrared liquid crystal spatial light modulators. *Thin Solid Films* **660**, 411–420 (2018).
- Tohsophon, T., Dabirian, A., De Wolf, S., Morales-Masis, M. & Ballif, C. Environmental stability of high-mobility indium-oxide based transparent electrodes. *APL Mater.* **3**, 116105 (2015).
- Morales-Masis, M. et al. Highly conductive and broadband transparent Zr-doped In₂O₃ as front electrode for solar cells. *IEEE J. Photovolt.* **8**, 1202–1207 (2018).
- Silva,  . Pd, Chaves, M., Durrant, S. F., Lisboa-Filho, P. N. & Bortoletto, J. R. Morphological and electrical evolution of ZnO: Al thin films deposited by RF magnetron sputtering onto glass substrates. *Mater. Res.* **17**, 1384–1390 (2014).
- Dhokal, T. et al. Transmittance from visible to mid infra-red in AZO films grown by atomic layer deposition system. *Sol. Energy* **86**, 1306–1312 (2012).
- Datta, I., Phare, C. T., Dutt, A., Mohanty, A. & Lipson, M. Integrated graphene electro-optic phase modulator. In *Conference on Lasers Electro-Optics, STu3N.5* (OSA, Washington DC, 2017).
- Yariv, A. Universal relations for coupling of optical power between microresonators and dielectric waveguides. *Electron. Lett.* **36**, 321–322 (2000).
- Amin, R. et al. Sub-wavelength GHz-fast broadband ITO Mach–Zehnder modulator on silicon photonics. *Optica* **7**, 333–335 (2020).

Acknowledgements

We acknowledge fruitful discussions with S. Chae, X. Xu, K. Yao, J. Schuck and E. Hwang, as well as experimental support from L. D'Cruz. This work was primarily supported by the NSF MRSEC Program at Columbia in the Center for Precision-Assembled Quantum Materials (DMR-201173 and DMR-1420634), in partnership with the National Research Foundation of Korea through the Global Research Laboratory (GRL) program (2016K1A1A2912707) and Research Fellow program (2018R1A6A3A11045864). Device characterization was supported by the National Science Foundation through the CAREER Award (ECCS-1752401). This work was performed in part at the Advanced Science Research Center NanoFabrication Facility at the Graduate Center of the City University of New York and in part at the Columbia Nano Initiative (CNI) Shared Lab Facilities at Columbia University. Synthesis of hBN (K.W. and T.T.) was supported by the MEXT Element Strategy Initiative to Form Core Research Center (grant number JPMXP0112101001) and the CREST(JPMJCR15F3), JST.

Author contributions

M.S.C., A.N. and Y.J. designed and conducted the initial experiments under the supervision of J.H. and J.T.T. M.S.C. and A.N. stacked, fabricated and conducted the electrical, optical and material characterizations of the samples with B.S.Y.K.'s contribution. B.S.Y.K. established a model for a work-function-mismatch-based doping mechanism. M.E.Z. and X.Z. contributed to the transmittance measurement of CVD samples. I.D. and M. Lipson contributed to the optical loss measurements of TOS-doped graphene integrated into the SiN waveguide. A.B. contributed to the doping study of DNTT. B.K. and D.R. provided flux-grown WSe₂ crystals. A.J. and A.N.P. provided the SWCNT grown on SiO₂/Si. Z.A.L. and I.K. provided the grown DNTT on TOS. M. Lee

contributed to the sample preparation. A.Z. contributed to the transmission electron microscopy, SAED and energy-dispersive X-ray spectroscopy measurements. M.N.N. contributed to the XPS measurements of CVD samples. T.T. and K.W. provided the hBN crystals. W.J.Y. contributed to discussions of the results. M.S.C., A.N. and B.S.Y.K. wrote the manuscript under the supervision of J.H. and J.T.T.

Competing interests

M.S.C., A.N., A.B., Y.J., J.H. and J.T.T. have filed for a US non-provisional patent application no. 17/236,404 regarding the technology reported in this article. The remaining authors declare no competing interests.

Additional information

Supplementary information The online version contains supplementary material available at <https://doi.org/10.1038/s41928-021-00657-y>.

Correspondence and requests for materials should be addressed to James Hone or James T. Teherani.

Peer review information *Nature Electronics* thanks Jin Sik Choi and the other, anonymous, reviewer(s) for their contribution to the peer review of this work.

Reprints and permissions information is available at www.nature.com/reprints.

Publisher's note Springer Nature remains neutral with regard to jurisdictional claims in published maps and institutional affiliations.

© The Author(s), under exclusive licence to Springer Nature Limited 2021